

1 **Convection in the Magnetosphere-Ionosphere System:**  
2 **a Multi-Mission Survey of its Response to IMF  $B_y$**   
3 **Reversals**

4 **N. A. Case<sup>1</sup>, A. Grocott<sup>1</sup>, R. C. Fear<sup>2</sup>, S. Haaland<sup>3,4</sup>, and J. H. Lane<sup>1</sup>**

5 <sup>1</sup>Department of Physics, Lancaster University, Lancaster, UK

6 <sup>2</sup>School of Physics & Astronomy, University of Southampton, Southampton, UK

7 <sup>3</sup>Max Planck Institute for Solar System Research, Göttingen, Germany.

8 <sup>4</sup>Birkeland Centre for Space Science, University of Bergen, Norway.

9 **Key Points:**

- 10 • Flows in the the magnetotail lobes respond promptly to changes in the IMF  $B_y$   
11 orientation, reaching a new state within 30-40 min.  
12 • No clear flow response is detected on timescales of up to four hours in the plasma  
13 sheet.  
14 • Ionospheric flows exhibit clear responses at higher latitudes and a less pronounced  
15 responses at lower latitudes.

---

Corresponding author: N. A. Case, [n.case@lancaster.ac.uk](mailto:n.case@lancaster.ac.uk)

**Abstract**

Past studies have demonstrated that the interplanetary magnetic field (IMF)  $B_y$  component introduces asymmetries in the magnetosphere-ionosphere (M-I) system, though the exact timings involved are still unclear with two distinct mechanisms proposed. In this study, we statistically analyze convective flows from three regions of the M-I system: the magnetospheric lobes, the plasma sheet, and the ionosphere. We perform superposed epoch analyses on the convective flows in response to reversals in the IMF  $B_y$  orientation, to determine the flow response timescales of these regions. We find that the lobes respond quickly and reconfigure to the new IMF  $B_y$  state within 30-40 min. The plasma sheet flows, however, do not show a clear response to the IMF  $B_y$  reversal, at least within four hours post-reversal. The ionospheric data, measured by the SuperDARN radar network, match their counterpart magnetospheric flows, with clear and prompt responses at  $\geq 75^\circ$  MLAT but a less pronounced response at 60–70 MLAT. We discuss the potential implication of these results on the mechanisms for introducing the IMF  $B_y$  component into the M-I system.

**1 Introduction**

The Earth’s magnetosphere and ionosphere are intrinsically coupled, with the processes and dynamics in one linked to the processes and dynamics of the other via electric fields, magnetic field-aligned currents, and particle exchange (Blanc, 1988). This magnetosphere-ionosphere (M-I) system is also coupled with the external driving of the solar wind and the embedded interplanetary magnetic field (IMF). Changes in the upstream driving, for example in the solar wind dynamic pressure or the orientation of the IMF, induce changes into the M-I system as a whole.

Past studies have clearly demonstrated that the orientation of the east-west component of the interplanetary magnetic field, more commonly referred to as the IMF  $B_y$  component, controls many different aspects of the magnetosphere-ionosphere system. For example, a non-zero IMF  $B_y$  component shifts the site of dayside reconnection (Park et al., 2006), introduces twisting of the magnetotail (e.g., Russell, 1972; Cowley, 1981), and produces directionally-dependent fast flows in the magnetotail associated with untwisting (Grocott et al., 2007; Pitkänen et al., 2013). In the ionosphere, the IMF  $B_y$  component drives asymmetries in the aurora (e.g., Østgaard et al., 2004; Reistad et al., 2013), including in transpolar arcs (e.g., Fear & Milan, 2012), and forms large-scale morphological changes to the ionospheric convection patterns (e.g., Ruohoniemi & Greenwald, 2005; Grocott, 2017).

Large-scale convection in the Earth’s magnetosphere is primarily driven by dayside reconnection as described by the Dungey cycle (Dungey, 1961). Under southward IMF conditions, newly opened field lines transfer from the dayside magnetopause, across the polar cap, and into the nightside magnetotail. Once in the magnetotail, the field lines are forced down to the neutral sheet region, where they reconnect with oppositely directed field lines from the opposite lobe and propagate earthward. Due to the pile up in the nightside near-Earth region, the field lines then convect around the Earth back to the dayside, where the cycle repeats. In the magnetotail, convective flows are primarily in the duskward direction in the pre-midnight sector and dawnward in the post-midnight sector (e.g. Hori et al., 2000; Kissinger et al., 2012).

Under non-zero IMF  $B_y$  conditions, certain asymmetries in the M-I system’s convective flows develop. At the dayside magnetopause, the region of maximum shear and reconnection is shifted northward in the dusk sector and southward in the dawn sector for positive IMF  $B_y$ . For Negative  $B_y$  the shift is reversed. In the lobes, this asymmetric flux loading results in a net flow across the noon-midnight meridian whose direction is dependent upon the orientation of the IMF  $B_y$  component (Cowley, 1981; Haaland et al., 2008; Case et al., 2018). In the Northern Hemisphere, under IMF  $B_y > 0$  con-

67 ditions, flows are predominantly in the +Y direction, and in the Southern Hemisphere  
 68 are predominantly in the -Y direction. When the IMF  $B_y$  orientation is reversed, so too  
 69 are the predominate flow directions (Haaland et al., 2008; Case et al., 2018). Since the  
 70 ionosphere and magnetosphere are intrinsically linked, asymmetries in the ionospheric  
 71 convection are also created when there is an IMF  $B_y$  component present. Large scale dif-  
 72 ferences in the ionospheric potentials are observed, creating different flow patterns (con-  
 73 sisting of a number of distinct “cells”) whose morphologies and size are dependent upon  
 74 the IMF  $B_y$  orientation (e.g., Cowley & Lockwood, 1992; Ruohoniemi & Greenwald, 2005)  
 75 and hemisphere (e.g. Pettigrew et al., 2010). In particular, the anti-sunward flow across  
 76 the polar cap is deflected by the IMF  $B_y$  component, resulting in the Y-component of  
 77 the flow switching orientation in response an IMF  $B_y$  reversal (Haaland et al., 2007).

78 In the plasma sheet too, the average convective flow develops an interhemispheric  
 79 asymmetry under non-zero IMF  $B_y$  conditions, with the flows being preferentially di-  
 80 rected in opposite directions in the two hemispheres based on the orientation of the IMF  
 81  $B_y$  component (Pitkänen et al., 2019).

82 The  $B_y$  component of the IMF which is imparted on the dayside field lines is trans-  
 83 ferred into the nightside too, though the timescales and mechanisms for this remain un-  
 84 clear (e.g., Case et al., 2018). For example, studies by Fear and Milan (2012) and Browett  
 85 et al. (2017) have shown that the effect of the IMF  $B_y$  component is introduced into the  
 86 tail on timescales that match the traditional Dungey-cycle driven picture (e.g. 2-4 hrs)  
 87 presented by Cowley (1981) and Cowley and Lockwood (1992) (hereafter referred to as  
 88 the “Cowley explanation”). However, recent work has also shown that the  $B_y$  compo-  
 89 nent could be introduced on much shorter timescales through pressure forces on the in-  
 90 ner magnetotail (e.g., Khurana et al., 1996; Tenfjord et al., 2015, 2017) (hereafter referred  
 91 to as the “Tenfjord explanation”). The result of both of these methods, however, is the  
 92 same: a twisting of the magnetotail (e.g., Russell, 1972; Cowley, 1981) which, in turn,  
 93 creates an asymmetry in the flow direction as field lines convect back around to the day-  
 94 side (e.g., Grocott et al., 2007).

95 When attributing phenomena or the responses of certain regions to a particular IMF  
 96  $B_y$  state, previous studies have used a range of times over which to average the IMF  $B_y$   
 97 component. For example, Pitkänen et al. (2013, 2017) used a 130 min average of the IMF  
 98  $B_y$  preceding their “fast flow” events in the plasma sheet for characterization of these  
 99 events. Others have used, or have suggested, timescales ranging from 45 min to over 3 hours  
 100 for the IMF  $B_y$  component to propagate into the tail (e.g., Fear & Milan, 2012; Pitkänen  
 101 et al., 2016; Browett et al., 2017). The Tenfjord explanation, however, in which infor-  
 102 mation is thought to be propagated by pressure waves rather than ‘penetration’, is pro-  
 103 posed to operate with time scales of the order of 15 minutes.

104 Additionally, there is some ambiguity around what is defined as a response. There  
 105 is both a *response time*, in which the magnetosphere or ionosphere starts to change based  
 106 on the new IMF  $B_y$  orientation (which itself has to be time lagged from the bowshock  
 107 to the magnetopause), and then a *reconfiguration time*, in which the magnetosphere or  
 108 ionosphere has reached its “end state” based on this new orientation. Some studies have  
 109 attempted to address this, e.g. Grocott and Milan (2014) and Tenfjord et al. (2017). Grocott  
 110 and Milan (2014), for example, showed that the ionosphere could respond quickly to changes  
 111 in the IMF but took much longer to fully reconfigure. Other studies, such as modeling  
 112 work by Kabin et al. (2003), however, showed much shorter reconfiguration times (15-  
 113 20 min).

114 Determining a response time is further complicated by the possibility that the re-  
 115 sponse time of a particular magnetotail phenomenon may occur on a different timescale  
 116 to that of simply introducing the IMF  $B_y$  component into the magnetotail. For exam-  
 117 ple, as discussed in Cowley (1981), the convection of the IMF field lines with a  $B_y$  into  
 118 the magnetotail produces a non-uniform distribution (in the Y-Z plane) of open field lines

119 crossing the magnetopause. This results in a torque which, in turn, twists the magne-  
 120 totail. One can envisage that the twisting of the magnetotail may take far less time to  
 121 develop than the time required for the effects of the IMF  $B_y$  component to be fully in-  
 122 troduced into the tail, if only a small amount of torque is required to develop this twist.  
 123 In such a scenario, the required torque may be sufficiently provided by the newly intro-  
 124 duced  $B_y$  component in the lobes well before the  $B_y$  component has fully developed in  
 125 the tail. Alternatively, the tail twisting time may be longer than the time required for  
 126 the  $B_y$  component to be introduced if a large amount of torque were to be required - whether  
 127 this be to simply develop a twist or to overcome a previously twisted state. In this sce-  
 128 nario, it may take some period of time after the  $B_y$  component has been fully introduced  
 129 for sufficient torque to be applied to twist the tail. In Case et al. (2018), the effect of tail  
 130 twisting became most obvious during longer timescale averages, though several tail twist-  
 131 ing intervals were found that occurred on short timescales. We note that this result is  
 132 not, however, inconsistent with the Cowley (1981) interpretation since it could indicate  
 133 that the neutral sheet can twist as a result of IMF  $B_y$  being introduced into the lobes  
 134 only.

135 The excitation of a flow in the Y-direction ( $V_y$ ) or in the Y-component of the field-  
 136 perpendicular direction ( $V_{\perp y}$ ) is linked to the introduction of the IMF  $B_y$  component  
 137 into the magnetotail, though it is in itself a separate effect to be studied. In the lobes,  
 138  $V_y$  is introduced by asymmetric flux loading, with continued loading introducing asym-  
 139 metric pressure driving convection. In the plasma sheet, on closed magnetic field lines, the  
 140 differences between the Tenfjord and Cowley explanations becomes clear. In the Ten-  
 141 fjord case, one should expect rapid responses in  $V_{\perp y}$ . As the pressure wave from the lobes  
 142 transfers through to the closed field line region, it must introduce a convective plasma  
 143 flow. In the Cowley picture, however, no such pressure wave exists and instead the  $B_y$   
 144 component is introduced through the Dungey cycle process. As such it takes much longer  
 145 for the  $B_y$  introducing field lines to propagate into the closed field line regions, where,  
 146 through  $\vec{E} \times \vec{B}$  drift, a  $V_{\perp y}$  is introduced (e.g. Juusola et al. (2011); Pitkänen et al. (2017)  
 147 and references therein).

148 The focus of the present study is to investigate the time it takes for the M-I sys-  
 149 tem to respond to the introduction of an IMF  $B_y$  component. Particularly, we investi-  
 150 gate the response of magnetospheric and ionospheric convection to reversals in the ori-  
 151 entation of the IMF  $B_y$  component through a series of superposed epoch analyses. In  
 152 the following, we undertake such analyses for the magnetospheric lobes (Section 3.1), the  
 153 magnetotail plasma sheet (Section 3.2), and ionosphere (Section 3.3).

## 154 2 Data

155 The data used in this study are collected from three separate, but linked, regions,  
 156 namely the magnetospheric lobes, the ionosphere, and the plasma sheet. Data are col-  
 157 lated from several different magnetospheric spacecraft missions: Geotail (Nishida, 1994),  
 158 Cluster (Escoubet et al., 1997), and THEMIS (Angelopoulos, 2009), along with data from  
 159 the Super Dual Auroral Radar Network (SuperDARN) (Chisham et al., 2007).

160 Cluster’s Electron Drift Instrument (EDI) (Paschmann et al., 1997) is used to study  
 161 the flows within the night-side magnetotail lobes. EDI is the preferred instrument to study  
 162 convection here, rather than Cluster’s Ion Spectrometry (CIS) instrument (Rème et al.,  
 163 2001) for example, due to the relative low density of the plasma in this region and space-  
 164 craft charging effects. We use data where the EDI instrument flags (Georgescu et al.,  
 165 2010) suggest that it is working as intended (i.e. in the low density lobe region) but fur-  
 166 ther restrict data to the nightside lobes ( $X_{GSM} < 0R_E$ ,  $|Y_{GSM}| < 15R_E$ , and  $|Z_{GSM}| >$   
 167  $1R_E$ ) and remove flows with a velocity greater than  $100 \text{ kms}^{-1}$ , as these are likely to be  
 168 anomalous (Haaland et al., 2008). Lobe data are also classified by hemisphere using the  
 169 local  $B_x$  component (i.e.  $B_x > 0$  in the northern hemisphere). We note that since EDI

170 measures perpendicular drift of an electron beam gyro center, the velocity it measures  
 171 is the true convection velocity, i.e.  $V_y \equiv V_{\perp y}$ . EDI data coverage spans years 2001-2015  
 172 inclusive for spacecraft 1 and 3, and 2001-2004 inclusive for spacecraft 2. No EDI data  
 173 are available for spacecraft 4.

174 The CIS experiment is used to determine convection within the high-density plasma  
 175 sheet region where measurement errors due to spacecraft charging or low sample rates  
 176 are negligible. The ion Electrostatic Analyzer (iESA) (McFadden et al., 2008) on-board  
 177 THEMIS and the Low Energy Proton (LEP) instrument (Mukai et al., 1994) on-board  
 178 Geotail are also used to compliment the plasma sheet data from Cluster. This combined  
 179 plasma sheet dataset is reduced to only incorporate measurements recorded between  $-50R_E <$   
 180  $X_{GSM} < -14R_E$ ,  $|Y_{GSM}| < 15R_E$ , and  $|Z_{GSM}| < 5R_E$  and with a corresponding  
 181 plasma beta of greater than 0.1. Data coverage spans years 2001-2014 for Cluster CIS  
 182 (spacecraft 1 and 3 only), 2007-2019 for Themis, and 1992-2016 for Geotail. All space-  
 183 craft data are resampled to one minute resolution and are presented in GSM coordinates.

184 Ionospheric convection data, for years 1999-2016 inclusive, are obtained from the  
 185 SuperDARN radar network. The 35 SuperDARN radars currently in operation are used  
 186 predominantly to study plasma convection in the high-latitude ionosphere in both the  
 187 northern and southern hemispheres (Chisham et al., 2007). In addition to the raw line-  
 188 of-sight data from each radar, fitted global convection maps, produced using spherical  
 189 harmonic functions via the ‘‘Map Potential’’ procedure, are available (Ruohoniemi & Baker,  
 190 1998). These global maps allow the modelled plasma convection from any point in the  
 191 modelled regime to be determined - even if there are no line-of-sight data in that region.  
 192 This useful feature, however, makes using global maps unsuitable when looking at lo-  
 193 calised regions, as the map could have been derived from relatively few data points that  
 194 are not located near the region of interest. Additionally, the global maps incorporate sta-  
 195 tistical averages that utilize the IMF  $B_y$  component to derive their shape and so any flows  
 196 derived from these maps would naturally respond to an IMF  $B_y$  reversal.

197 To overcome these issues, we use a local fitting method, as described by Thomas  
 198 and Shepherd (2018), to produce localised convection fits that are not dependent on large-  
 199 scale statistical averages or pre-determined by the orientation of the IMF. The Thomas  
 200 and Shepherd (2018) method involves solving for a best-fit velocity within a magnetic  
 201 latitude - longitude (MLAT-MLT) cell by performing a least squares linear regression  
 202 to all available line-of-sight vectors. This procedure is similar to the technique that com-  
 203 bined instantaneous line-of-sight velocity measurements from a pair of radars with over-  
 204 lapping beams described by Hanuise et al. (1993). Like Thomas and Shepherd (2018),  
 205 we impose a minimum azimuth separation of  $25^\circ$  in order to calculate a merged vector  
 206 at a given location. Since we are studying the effect of IMF  $B_y$  reversals on the iono-  
 207 spheric convection, we have far fewer intervals than Thomas and Shepherd (2018) had  
 208 in their IMF-driven analysis. To further enhance the number of measurements available  
 209 for our analysis, we perform the local fit to a region  $8^\circ$  of latitude square (i.e. a square  
 210 whose sides are equal to the equivalent length of  $8^\circ$  of latitude at that location), such  
 211 that there are anywhere up to 5500 measurements used in each fit.

212 Further, we note that the size and shape of the ionospheric convection pattern is  
 213 dependent upon geomagnetic activity. This introduces some uncertainty when compar-  
 214 ing the MLAT of the flows with conjugate regions of the magnetosphere. In an effort to  
 215 address this, we remove any extreme cases, such as a particularly enlarged or shrunken  
 216 pattern, by restricting the SuperDARN data to intervals where the corresponding Kp  
 217 index is  $\geq 3$  and  $< 5$  (Milan, Evans, & Hubert, 2010). Additionally, we filter the data  
 218 to intervals where the westward auroral electrojet index (AL) is  $< -200$ nT to remove  
 219 particularly strong auroral events which may suppress, or otherwise influence, the iono-  
 220 spheric flows.

221

## 2.1 IMF $B_y$ Reversals

222

223

224

225

226

227

228

229

230

231

To determine the time taken for the magnetospheric and ionospheric flows to respond to changes in the IMF  $B_y$  component, we perform superposed epoch analyses with respect to IMF  $B_y$  reversals. As described in Case et al. (2018), during a reversal the IMF  $B_y$  state promptly switches from one orientation to the other, having both been steady before the switch and remaining steady (but oppositely orientated) after it. In this study, we simply define a reversal as having occurred if the mean IMF  $B_y$  component over the 20 min period after a timestamp is oppositely directed to the 20 min mean before that timestamp. If several subsequent timestamps fulfil this criteria, the middle value of this series is taken as the reversal time. Altering the length of time we average over (e.g. 20 min) does not seem to significantly alter the number, or quality, of reversals.

232

233

234

235

236

237

238

239

240

241

Solar wind and associated IMF data, for years 1992-2019 inclusive, are provided by the high-resolution (1 min) OMNIweb dataset. These data have been time-lagged to account for the propagation delay between their upstream observer (e.g. WIND, ACE, DSCOVR) and the Earth's bowshock (King & Papitashvili, 2005). We note that, whilst statistically valid, individual propagation estimates can be inaccurate (e.g., Mailyan et al., 2008; Case & Wild, 2012; Vokhmyanin et al., 2019). Additionally, the time taken for the shocked solar wind to traverse from the bowshock to the magnetopause is variable and is not accounted for in the OMNI dataset. Since we do not attempt to account for this extra delay either, we expect that any responses to the IMF  $B_y$  reversals will be offset by 5 to 15 min (Khan & Cowley, 1999).

242

243

244

245

246

247

From the OMNI dataset, a subset of 5,767 positive to negative IMF  $B_y$  reversals are found, and a set of 5,798 negative to positive reversals. In the following analyses, observations from the magnetosphere and ionosphere contemporaneous data to these reversals are collated and averaged. We note that not all of the IMF  $B_y$  reversals have coincident spacecraft or ionospheric data, due to the data coverage of those data sets and the suitability of the spacecraft locations.

248

## 3 Results

249

### 3.1 Lobe Flows

250

251

252

253

254

255

256

Plotted in Figure 1 is a superposed epoch analysis of the convection velocity in the night-side magnetotail lobes, as recorded by Cluster's EDI instruments. Data recorded from 30 min before an IMF  $B_y$  reversal and up to 60 min after a reversal are temporally aligned and their mean is computed. In panels (a) and (b), the data correspond to a positive to negative IMF  $B_y$  reversal and were collected in the northern (NH) and southern hemisphere (SH) respectively. In panels (c) and (d), the data correspond to a negative to positive IMF  $B_y$  reversal.

257

258

259

260

261

Shown by the thin gray line is the mean for each superposed timestamp. The gray shaded region indicates the standard error of that mean. Plotted with a thick black line are the smoothed means (10 point moving average centered on the timestamp). Plotted in olive green, and shown on the secondary y-axis, are the number of data points that went into each timestep average.

262

263

264

265

266

Plotted in Figure 1a, is a superposed epoch analysis of lobe flows in the northern hemisphere with respect to positive to negative IMF  $B_y$  reversals. The average  $V_y$  flow is positive, remaining steady around  $+2.5 \text{ km s}^{-1}$  until the IMF  $B_y$  reverses orientation. The average  $V_y$  flow decreases, though does not quite become negative, after the IMF  $B_y$  reversal and reaches a minimum state between 20-30 min.

267

268

In panel b, a superposed epoch analysis is shown for the same IMF  $B_y$  reversal type as panel a but with data from the southern hemisphere. The trend is broadly opposite

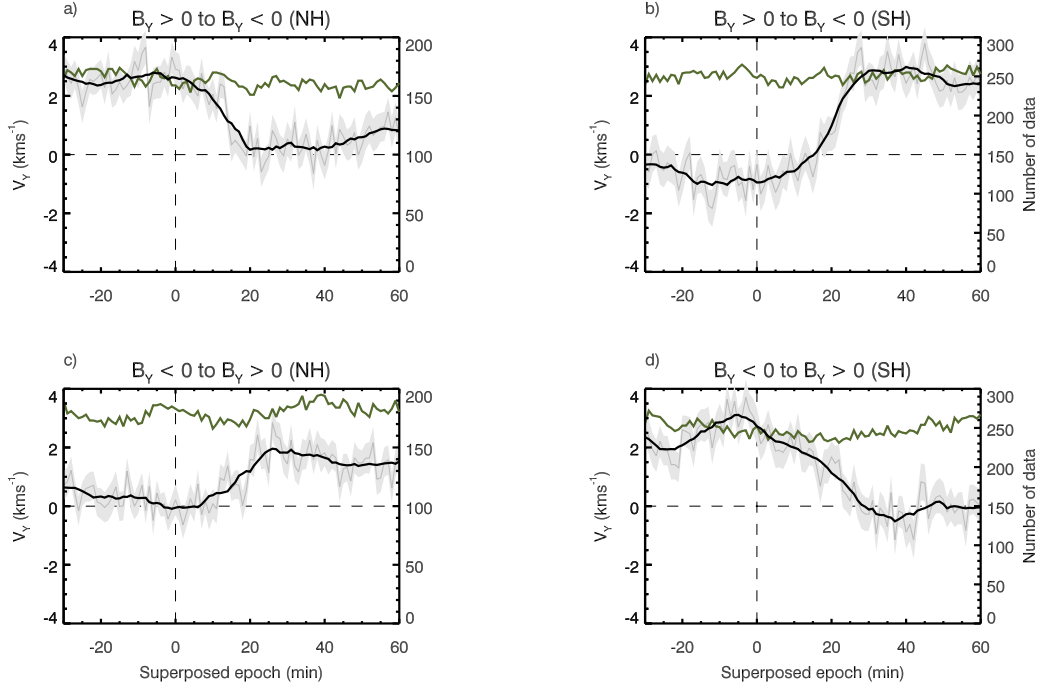


**Figure 1.** Superposed epoch Cluster-EDI velocity data sampled in the lobes are shown for (a and b) IMF  $B_y$  positive to negative reversals and for (c and d) IMF  $B_y$  negative to positive reversals. (a and c) Northern Hemisphere (NH) and (b and d) Southern Hemisphere (SH) data are shown respectively. Plotted in black are the smoothed superposed means for all data. The gray line shows the unsmoothed means and the gray shaded regions indicate the standard error of the mean for each timestamp. The number of data points for each superposed average timestamp is shown by the olive green line on the secondary y-axis.

269 to that shown in panel a, with an average  $V_y$  of around  $-1 \text{ km s}^{-1}$  under positive IMF  
 270  $B_y$ , steadily increasing after the reversal to around  $+3 \text{ km s}^{-1}$  under negative IMF  $B_y$ .  
 271 Again, the  $V_y$  flows reach a maximum state around 30 min after the reversal occurs.

272 Panel c is again for  $V_y$  data in the northern hemisphere lobe, though this time as-  
 273 sociated with an IMF  $B_y$  negative to positive reversal. Its trend is almost opposite to  
 274 the trend in panel a (i.e. opposite IMF  $B_y$  reversal type but same hemisphere) and broadly  
 275 the same as the trend in panel b (i.e. opposite reversal type and opposite hemisphere).  
 276 The average  $V_y$  lobe flow is around zero under negative IMF  $B_y$  steadily increasing to  
 277 around  $+2 \text{ km s}^{-1}$  under positive IMF  $B_y$ , with this maximum being reached around 30-  
 278 40 min after the reversal occurs.

279 In panel d,  $V_y$  data from the southern hemisphere for the IMF  $B_y$  negative to pos-  
 280 itive reversal is shown. Its trend is almost exactly opposite to that in panel b (i.e. op-  
 281 posite IMF  $B_y$  reversal type but same hemisphere) and broadly the same as the trend  
 282 in panel a (i.e. opposite reversal type and opposite hemisphere). The average lobe  $V_y$   
 283 flow is around  $+2 \text{ km s}^{-1}$  under negative IMF  $B_y$  and steadily decreases to around  $-1$   
 284  $\text{km s}^{-1}$  30 min after the reversal occurs.

285 From the above plots, we also note a persistent asymmetry, with a generally pos-  
 286 itive  $V_y$ . We also note slightly different  $V_y$  magnitude changes between the northern and  
 287 southern hemispheres, as well as differences between positive to negative and negative

288 to positive IMF  $B_y$  reversals. A detailed study of these features is beyond the scope of  
 289 the present paper, but differences in the magnetospheric response between IMF  $B_y >$   
 290 0 and IMF  $B_y <$  0 states have been discussed recently (e.g. Holappa & Mursula, 2018;  
 291 Liou et al., 2020; Reistad et al., 2020).

### 292 3.1.1 IMF $B_z$ dependence

293 In the following, the lobe flows presented in Figure 1 have been further split based  
 294 upon the 30 min median IMF  $B_z$ . Additionally, to account for the fact that the IMF  $B_z$   
 295 orientation may also reverse alongside the IMF  $B_y$  orientation, we require that 80% of  
 296 data that make up the average match the sign of the average. In Figure 2, the super-  
 297 posed epoch of flows with an associated positive median IMF  $B_z$  is plotted with the blue  
 298 line and negative IMF  $B_z$  with the red line. The red and blue “error bars” show the stan-  
 299 dard errors of the mean of each timestamp average and the black line shows the mean  
 300 for all data. The red and blue histograms show the total amount of data for their respec-  
 301 tive classifications.

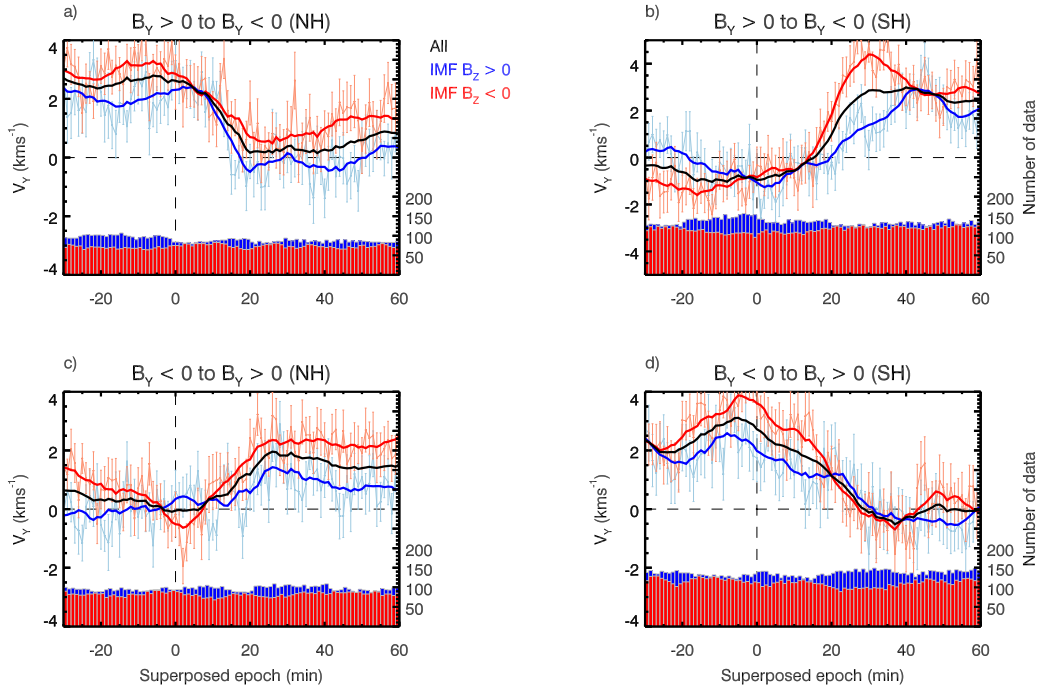


**Figure 2.** In the same format as Figure 1, superposed epoch Cluster-EDI velocity data sam-  
 pled in the lobes are shown for (a and b) IMF  $B_y$  positive to negative reversals and for (c and  
 d) IMF  $B_y$  negative to positive reversals. (a and c) Northern Hemisphere (NH) and (b and d)  
 Southern Hemisphere (SH) data are shown respectively. Plotted in blue and red are data for  
 positive and negative IMF  $B_z$  respectively.

302 In general, the IMF  $B_z$  orientation alone appears to have little effect on the over-  
 303 all trends, with changes in the direction of the lobe  $V_y$  being consistent regardless of IMF  
 304  $B_z$ .



305

### 3.1.2 Solar wind speed dependence

306

307

308

309

310

311

312

We have also split the lobe flows presented in Figure 1 based upon the 30 min median solar wind velocity  $V_{sw}$ . In Figure 3, the superposed epoch of flows with an associated median  $V_{sw} < 450 \text{ km s}^{-1}$  (“slow”) is plotted with the blue line and  $V_{sw} \geq 450 \text{ km s}^{-1}$  (“fast”) with the red line. The red and blue “error bars” show the standard errors of the mean of each timestamp averaged and the black line shows the mean for all data. The red and blue histograms show the total amount of data for their respective classifications.

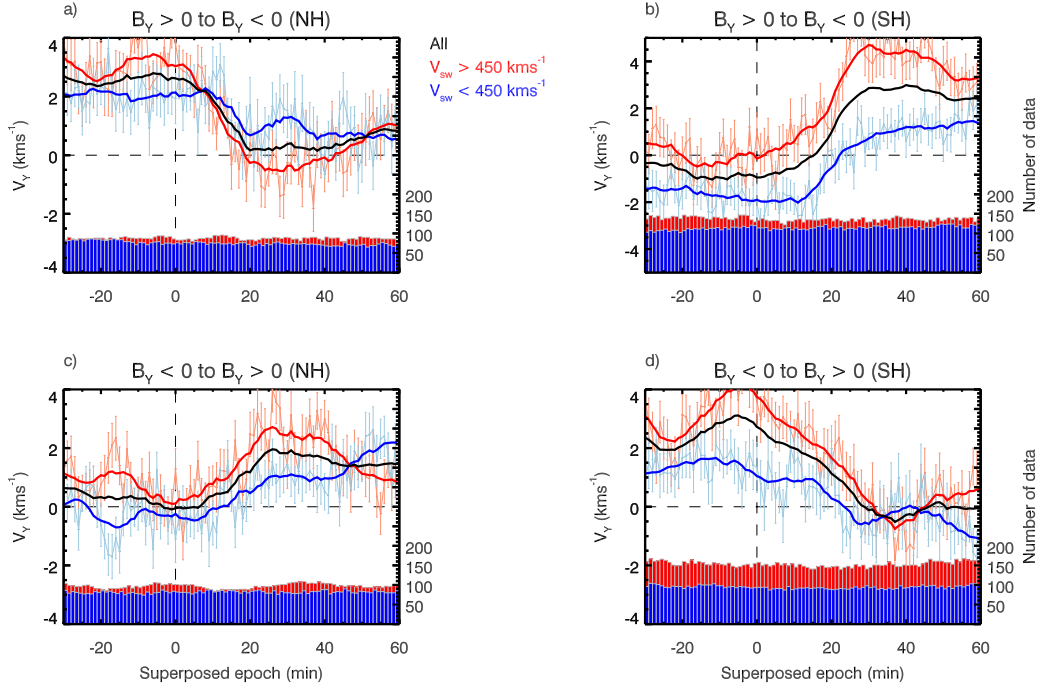


**Figure 3.** In the same format as Figure 1, superposed epoch Cluster-EDI velocity data sampled in the lobes are shown for (a and b) IMF  $B_y$  positive to negative reversals and for (c and d) IMF  $B_y$  negative to positive reversals. (a and c) Northern Hemisphere (NH) and (b and d) Southern Hemisphere (SH) data are shown respectively. Plotted in blue and red are data for  $V_{sw} < 450 \text{ km s}^{-1}$  and  $V_{sw} \geq 450 \text{ km s}^{-1}$  respectively.

313

314

315

316

317

318

319

As with the IMF  $B_z$  orientation, it appears that the solar wind velocity alone has little affected on the overall trends, with changes in the direction of the lobe  $V_y$  being largely consistent for both fast and slow  $V_{sw}$ . However, the lobe  $V_y$  flows are, in general, more consistently displaced towards positive  $V_y$  for fast solar wind when compared with slow solar wind. The only exception to this is in panel a, under negative IMF  $B_y$ , where the lobe flows associated with fast solar wind average around  $-0.5 \text{ km s}^{-1}$  whilst the flows associated with slow solar wind average around  $+1 \text{ km s}^{-1}$ .

320

### 3.1.3 Dayside reconnection rate dependence

321

322

323

324

The response of the magnetospheric system, including the lobes, to upstream driving is governed by a combination of factors - rather than just the solar wind velocity and IMF  $B_z$  previously analysed. To combine these two factors, however, is non-trivial. Slow solar wind may still be geo-effective if accompanied by a strongly negative  $B_z$ . Conversely,

325 a weakly negative IMF  $B_z$  may be geo-effective with a strong solar wind velocity. We  
 326 therefore utilise the dayside reconnection parameter,  $\Phi_D$ , of Milan et al. (2012) to bet-  
 327 ter combine the effects of these two parameters.

328 Milan et al. (2012) define the dayside reconnection rate,  $\Phi_D$ , as the magnetic flux  
 329 per unit of time converted from a closed topology to open topology, measured in volts.  
 330 Specifically, through their statistical analysis of the rate of growth of the auroral oval,  
 331 they determine the following expression for  $\Phi_D$  :

$$332 \quad \Phi_D = L_{eff}(V_x)V_x B_{yz} \sin^{9/2} \left( \frac{|\theta|}{2} \right) \quad (1)$$

333 where

$$334 \quad L_{eff}(V_x) = 3.8R_E \left( \frac{V_x}{4 \times 10^5 \text{ms}^{-1}} \right) \quad (2)$$

$$335 \quad \text{and } B_{yz} = \sqrt{B_y^2 + B_z^2} \text{ and } \theta = \tan^{-1} \left( \frac{B_y}{B_z} \right).$$

336 In Figure 4 we have split the lobe flows presented in Figure 1 based upon the day-  
 337 side reconnection rate  $\Phi_D$ . The superposed epoch of flows with an associated  $\Phi_D < 90$   
 338 kV is plotted with the blue line and  $\Phi_D > 100$  kV with the red line. The red and blue  
 339 “error bars” show the standard errors of the mean of each timestamp average and the  
 340 black line shows the mean for all data. The red and blue histograms show the total amount  
 341 of data for their respective classifications.

342 For enhanced dayside reconnection rates, i.e.  $\Phi_D > 100$  kV (red line in Figure 4),  
 343 we see a clear reversal in the lobe flow  $V_y$  component associated with the IMF  $B_y$  ori-  
 344 entation. The trend is broadly similar to that shown in Figure 1, with distinct reversals  
 345 in the flow direction starting almost immediately after a reversal and being complete within  
 346 around 30 min.

347 For decreased dayside reconnection rates, i.e.  $\Phi_D < 100$  kV (blue line in Figure 4),  
 348 we do not see such a clear response. The  $V_y$  flows are, in general, more suppressed than  
 349 their enhanced counterparts and their response is less distinct and more gradual.

### 350 3.2 Plasma Sheet Flows

351 Data from the Cluster CIS, Geotail LEP, and THEMIS iESA instruments are sel-  
 352 lected to provide flow data in the plasma sheet region ( $-50 < X_{GSM} < -14R_E$ ,  $|Y_{GSM}| <$   
 353  $7R_E$ ,  $|Z_{GSM}| < 3R_E$ ) with a corresponding plasma beta greater than 0.1. The flow data  
 354 are then further restricted to intervals of earthward flow ( $V_x > 0 \text{ kms}^{-1}$ ) since tailward  
 355 flow, predominantly the result of reconnection events, would be expected to occur in the  
 356 opposite Y-direction. Additionally, flows with a total velocity greater than  $500 \text{ kms}^{-1}$   
 357 are removed, as these are likely to be travelling too fast to be directly affected by any  
 358 induced IMF  $B_y$  effects (Juusola et al., 2011).

359 A superposed epoch analysis of the plasma sheet flows is presented in Figure 5, with  
 360 the same format as Figure 1, though extended up to four hours after an IMF  $B_y$  rever-  
 361 sal. In panels (a) and (b), the plotted data correspond to a positive to negative IMF  $B_y$   
 362 reversal and were collected in the northern (NH) and southern hemisphere (SH) respec-  
 363 tively. Since the neutral sheet is not stationary, and does not necessarily lie on the  $Z_{GSM} =$   
 364  $0$  axis, we use the  $B_x$  component of the local magnetic field to define whether the data  
 365 is in the NH or SH. In panels (c) and (d), the plotted data correspond to a negative to  
 366 positive IMF  $B_y$  reversal. The number of data points for each averaged timestamp is shown  
 367 by the olive green line on the secondary y-axis.

368 The results of the superposed epoch analyses for the plasma sheet are much less  
 369 clear than those for the lobes. On a short timescale, we see a reversal from  $V_y$  around  
 370  $-10 \text{ kms}^{-1}$  to  $+30 \text{ kms}^{-1}$  in panel a, occurring within 30 min of the reversal. Addition-  
 371 ally, in panel c (same hemisphere as panel a but opposite IMF  $B_y$  reversal) we see the  
 372 opposite occur, with  $V_y$  starting at around  $+20 \text{ kms}^{-1}$  and finishing reaching  $-20 \text{ kms}^{-1}$   
 373 at around 30 min of the reversal.

374 However, the reversals observed are of the same order as subsequent variations through-  
 375 out the complete 4 hr window. Additionally, corresponding reversals are not observed  
 376 in the southern hemisphere.

### 377 3.3 Ionospheric Flows

378 Convection in the ionosphere is intrinsically coupled to the convection of magnetic  
 379 flux in the magnetosphere. Ionospheric flows, therefore, provide another way of measur-  
 380 ing the large-scale convection of the magnetotail. As such, we utilise the SuperDARN  
 381 radar network to determine the corresponding ionospheric flows for the lobes and plasma  
 382 sheet regions. In the panels of the following figures, we present superposed epoch anal-  
 383 yses of the best-fit velocities from the SuperDARN radar network for  $8^\circ$  intervals in MLAT,  
 384 spanning from  $60^\circ$  MLAT in the dayside ionosphere along the noon-midnight meridian  
 385 and across the polar cap to  $60^\circ$  MLAT in the nightside ionosphere. Data are from the  
 386 Northern Hemisphere network only, which generally provides significantly better cover-  
 387 age than the Southern Hemisphere network particularly at lower latitudes. As mentioned  
 388 in section 2, the data are filtered to intervals of  $3 \leq \text{Kp} < 5$  and  $\text{AL} < -200\text{nT}$  to re-  
 389 move active periods.

390 Data corresponding to a positive to negative IMF  $B_y$  reversal are shown in Fig-  
 391 ure 6 and data corresponding to a negative to positive reversal are shown in Figure 7.  
 392 In both figures the average flow direction ( $\theta$ ) and magnitude ( $|V|$ ) are shown by the blue  
 393 and red lines respectively. The flow direction is determined by taking the tangent of the  
 394 average east- and north-components of the measured vectors (i.e. where  $\theta = 90^\circ$  is east-  
 395 ward flow and  $\theta = -90^\circ$  is westward) and is completely independent of any large-scale  
 396 fits or pre-determined convection patterns. We note that the average flow direction re-  
 397 verses over the pole as a result of the sign of  $v_{North}$  changing. The number of data points  
 398 in each averaged time stamp is shown by the gray line on the secondary axis.

399 The ionosphere poleward of  $75^\circ$  MLAT, where the field lines are predominantly open,  
 400 clearly responds to reversals in the IMF  $B_y$  orientation. For positive to negative IMF  
 401  $B_y$  reversals, the ionospheric flows are directed more eastward (i.e. toward  $90^\circ$ ). Con-  
 402 versely, for negative to positive IMF  $B_y$  reversals the ionospheric flows are directed more  
 403 westward (i.e. toward  $-90^\circ$ ). For example, compare the  $80^\circ$  MLAT on the dayside (12  
 404 MLT) panels during the two types of IMF  $B_y$  reversal. During a positive to negative re-  
 405 versal (Figure 6), the flow orientation is steady at  $-70^\circ$  during the positive IMF  $B_y$  in-  
 406 terval, before rapidly changing direction to  $+40^\circ$  around 30 min after the  $B_y$  reversal.  
 407 During a negative to positive reversal (Figure 7), flow orientation is steady at  $+45^\circ$  dur-  
 408 ing the negative IMF  $B_y$  interval, before rapidly changing direction and reaching  $-50^\circ$   
 409 around 30 min after the  $B_y$  reversal.

410 Equatorward of  $75^\circ$ , i.e. closed field lines that map to the plasma sheet region of  
 411 the magnetosphere, the response is less clear. In some cases, a response consistent with  
 412 the higher latitudes does seem evident (e.g.  $65^\circ$  and  $70^\circ$  MLAT at 1200 MLT in Figure 6),  
 413 however, in other cases no response is evident (e.g.  $65^\circ$  and  $70^\circ$  MLAT at 1200 MLT in  
 414 Figure 7). At  $60^\circ$  MLAT on the dayside, for both reversal types, the flows are incred-  
 415 ibly variable suggesting the IMF  $B_y$  has no direct control on the flows in this region.

416 As with the lobe data, the response time of the ionospheric flows, in the open field  
 417 line region, to an IMF  $B_y$  reversal is prompt. Flows start to change direction within 10-  
 418 15 min and have completed their response, reaching a new end state, within 30-40 min.

#### 419 4 Discussion

420 In this study, we have shown that the magnetotail lobes, in which the field lines  
 421 are connected to the IMF, respond promptly to reversals in the IMF  $B_y$  component. In  
 422 the plasma sheet, where the field lines are closed, the picture is more complex with no  
 423 obvious response to IMF  $B_y$  reversals. In the ionosphere, we find clear responses in the  
 424 flow direction at higher latitudes but a less clear response at latitudes below  $75^\circ$  MLAT.

425 When analysing how specific events or phenomena in the magnetosphere-ionosphere  
 426 system are driven by the IMF, previous studies have tended to either use or find an in-  
 427 terval of IMF for which the average state best matches their results. The length of this  
 428 interval has varied from study to study. For example, Juusola et al. (2011) used an IMF  
 429 averaging time of 30 min when studying plasma sheet convection and work by Tenfjord  
 430 et al. (2015, 2017) has suggested that the nightside magnetosphere could respond to changes  
 431 in the IMF  $B_y$  orientation on timescales as short as 15 min. However, longer time scales  
 432 have also been suggested. For example, Fear and Milan (2012) found an average of the  
 433 IMF  $B_y$  component 3-4 hours previously best matched the local time of transpolar arc  
 434 formation, and Browett et al. (2017) found that the  $B_y$  component in the tail best cor-  
 435 related with IMF conditions on timescales of 1.5 and 3 hours, depending on solar wind  
 436 conditions.

437 In a statistical study of “fast flow” events in the plasma sheet, Pitkänen et al. (2013)  
 438 investigated the effect of different time averaging on their correlations and found a 130 min  
 439 average of the IMF  $B_y$  preceding their fast flows resulted in the highest correlation with  
 440 their data. They also noted, however, that their correlations were generally high, regard-  
 441 less of averaging length chosen, and attributed this to the stability of the IMF  $B_y$  com-  
 442 ponent (e.g., Borovsky, 2008; Milan, Grocott, & Hubert, 2010). However, in a later study  
 443 investigating “slow flows”, Pitkänen et al. (2019) use a 15 min average taken 135 min  
 444 prior to the corresponding data measurement in the tail. They cite the result of Petrukovich  
 445 and Lukin (2018), who developed a linear regression model of the plasma sheet  $B_y$  com-  
 446 ponent with respect to the IMF  $B_y$  component using Geotail data, as justification for  
 447 this.

448 Of course, these studies all investigated different effects that can be introduced by  
 449 an IMF  $B_y$  component. It is therefore entirely possible that the responses of these sep-  
 450 arate effects will occur on different timescales. However, it still leaves the question of what  
 451 time should we average over when analysing events in the magnetotail that are driven  
 452 by the IMF  $B_y$  component or, perhaps critically, whether averaging over some interval  
 453 is appropriate at all? Particularly when the IMF  $B_y$  component may have remained steady  
 454 over many hours before the event occurs.

455 To help address this, in this study, we have specifically investigated intervals of IMF  
 456  $B_y$  reversals to remove any potential ambiguity in the response timings of convection due  
 457 to the stability effect of the IMF  $B_y$  component. During a reversal, the IMF  $B_y$  com-  
 458 ponent swaps orientation (e.g.  $B_y > 0$  to  $B_y < 0$ ) having been both steady before the  
 459 reversal and remaining so afterward (Case et al., 2018).

460 We note that, in the Tenfjord explanation, the rationale for a prompt introduction  
 461 of the IMF  $B_y$  into the magnetotail is magnetic tension forces inducing shear flows, in  
 462 the opposite direction to the untwisting flows commonly studied when examining asym-  
 463 metric magnetospheric dynamics (e.g. Grocott et al., 2007; Pitkänen et al., 2013; Reis-  
 464 tad et al., 2018), on the inner magnetosphere creating a twist on the field lines. Indeed,  
 465 Tenfjord et al. (2018) note that in their MHD modeling, the inner magnetosphere ( $X =$

466  $-6.7R_E$ ) responds first with the effect then propagating downtail (to a minimum of  $X =$   
 467  $-11R_E$  in their study). This suggests that  $V_y$  and  $V_{\perp y}$  should also respond on short timescales.  
 468 Although the Cowley explanation does suggest a prompt response in the lobes, it also  
 469 suggests longer timescales in the plasma sheet. Indeed, with the Cowley explanation, the  
 470 IMF  $B_y$  component is introduced into the tail as the result of the Dungey cycle and so,  
 471 in this case, both the  $B_y$  and  $V_{\perp y}$  response would propagate from downtail to the inner  
 472 nightside magnetosphere, such as found by Pitkänen et al. (2016).

473 In Figure 1, we analyse the response of the flows in the magnetotail lobes to reversals  
 474 in the IMF  $B_y$  component. The figure demonstrates that the Y-direction of flow in  
 475 the lobes is dependent upon the IMF  $B_y$  orientation. In the Northern Hemisphere, posi-  
 476 tive IMF  $B_y$  driving results in positive  $V_y$  on average and negative IMF  $B_y$  driving re-  
 477 sults in negative  $V_y$  on average. This general trend is reversed in the Southern Hemisphere.  
 478 This result is consistent with our understanding of the asymmetric flux loading in the  
 479 lobes (e.g., Cowley, 1981; Cowley & Lockwood, 1992). For example, both Haaland et al.  
 480 (2008) and Case et al. (2018) have previously shown how the lobe flows are directed with  
 481 respect to the IMF  $B_y$  orientation through in-situ convection measurements. In both these  
 482 studies, the average IMF  $B_y$  direction was used to classify the upstream conditions cor-  
 483 responding to each lobe flow. However, as previously noted, in this study we have in-  
 484 stead looked at lobe flows explicitly associated with IMF  $B_y$  reversals.

485 This important distinction allows us to determine the response time of the lobe flows  
 486 to changes in upstream driving, particularly in reversals of the orientation of the IMF  
 487  $B_y$  component. As shown in Figure 1, the flows start responding promptly ( $< 5$  min)  
 488 to reversals in the IMF  $B_y$  orientation and reach an equilibrium or “end state”, based  
 489 on the new orientation, within 30-40 min. We note that there is some inherent uncer-  
 490 tainty in such an analysis since our zero-epoch value, i.e. when the IMF  $B_y$  reversal oc-  
 491 curs, is not measured directly but is instead taken from the OMNI dataset which has been  
 492 time shifted to the bow shock rather than to the interaction region at the dayside mag-  
 493 netopause.

494 A prompt response in the magnetotail lobes is to be expected for both the Tenfjord  
 495 and Cowley mechanisms. Although we do not place any criteria on the orientation of the  
 496 IMF  $B_z$  component, in Figure 1, we still expect that at least some reconnection between  
 497 the IMF and magnetopause will occur, even if under northward IMF conditions (e.g.,  
 498 Kessel et al., 1996), and that the resultant newly opened field lines will quickly propa-  
 499 gate across the polar cap (e.g., Dungey, 1961). Additionally, previous studies such as Tenfjord  
 500 et al. (2018), have shown that there is little difference in response times for the intro-  
 501 duction of a  $B_y$  component for northward or southward IMF intervals in the inner mag-  
 502 netosphere. Indeed, when we split the Cluster EDI convection data by IMF  $B_z$  orien-  
 503 tation, as shown in Figure 2, we found little difference in the response times. This was  
 504 also true when we split by solar wind velocity - as shown in Figure 3. However, when  
 505 we split by dayside reconnection rate, we did see a clear difference between the response  
 506 of high and low reconnection rates. This indicates that it is the electromagnetic (e.g. Poynt-  
 507 ing flux), rather than kinetic, energy of the solar wind and IMF that controls the lobe  
 508 flows. We note that this prompt response of the lobes follows for both the Cowley and  
 509 the Tenfjord explanations for introducing a  $B_y$  component (and hence exciting  $V_y$  flows)  
 510 into the tail, as they both rely on IMF-magnetopause reconnection creating an asym-  
 511 metric flux loading of the lobes.

512 Although it is clear that flows in the lobe region of the magnetotail are quick to  
 513 respond to changes in the IMF  $B_y$  orientation, results from the plasma sheet are much  
 514 less clear. As shown in Figure 5, no significant trends are found for the flows in the plasma  
 515 sheet in relation to the reversal of the IMF  $B_y$  orientation. This appears to be in con-  
 516 trast to other studies, such as Grocott et al. (2007), Juusola et al. (2011) and Pitkänen  
 517 et al. (2013, 2017), who have demonstrated the existence of asymmetries in the plasma  
 518 sheet flows based on the IMF  $B_y$  orientation. Additionally, it appears to be in contrast

519 to both the Cowley (Cowley, 1981; Cowley & Lockwood, 1992) and the Tenfjord (Tenfjord  
 520 et al., 2015, 2017) explanations for  $V_y$  flows being excited in the magnetotail. With the  
 521 Tenfjord explanation, we should see a response in the plasma sheet on timescales of 30-  
 522 40 min. With Cowley explanation, we should see a response on the order of several hours  
 523 - since the introduction of a flow asymmetry on closed plasma sheet field lines requires  
 524 the complete Dungey cycle convection of IMF field lines.

525 We note that the number of data points presented in Figure 5 is low. Requiring  
 526 that a spacecraft is located within the exact region of interest around the time of an IMF  
 527  $B_y$  reversal is a difficult criterion to fulfil. Therefore, to validate these magnetospheric  
 528 findings we compliment the in situ spacecraft data with ionospheric flow data recorded  
 529 by the SuperDARN radars. Since the ionospheric flows are intrinsically tied to, though  
 530 not necessarily constrained by, the convection of magnetic field lines in the magnetosphere,  
 531 they provide an additional data source to investigate the response of the M-I system to  
 532 reversals in the IMF  $B_y$  component.

533 In Figures 6 and 7, we present the ionospheric flows recorded by the SuperDARN  
 534 radar network. We note that, as described in Section 2, these flows are the best-fit ve-  
 535 locities derived directly from the radar line of sight velocity measurements, rather than  
 536 estimates from the global best-fit Map Potential patterns often used. At  $\geq 75^\circ$  MLAT,  
 537 with field lines mapping out into the lobes, clear responses in the flow direction can be  
 538 seen to the reversal in IMF  $B_y$  orientation - matching the data recorded by the in situ  
 539 spacecraft. However at  $< 75^\circ$  MLAT, mapping out to the plasma sheet region, the re-  
 540 sponse is much less clear for both reversal types. In some instances, a response consis-  
 541 tent with higher latitudes does appear, though is somewhat weaker, whilst in other cases  
 542 no clear response is seen at all. Data coverage does not appear to be an issue here, with  
 543 over 1,000 data points for each superposed epoch interval. We therefore believe that we  
 544 can rule out data coverage as a potential explanation for the apparent discrepancy be-  
 545 tween past studies and the plasma sheet results presented here.

546 We believe that the lack of response observed in the plasma sheet, and its appar-  
 547 ent disagreement with previous studies, e.g. Juusola et al. (2011); Pitkänen et al. (2016),  
 548 could, in fact, be explained by the Dungey cycle. For example, in the Cowley explana-  
 549 tion (Cowley, 1981; Cowley & Lockwood, 1992) of introducing a  $B_y$  component into the  
 550 magnetotail, tail reconnection is needed to drive the introduced  $B_y$  field from the lobes  
 551 into the near-Earth plasma sheet. Tail reconnection is a pseudo-random event meaning  
 552 that when performing superposed epoch analyses, such as ours, its effects would be smeared  
 553 out - leading to no discernible result. Yet when one specifically looks for these  $B_y$ -related  
 554 flows in the tail, e.g. Pitkänen et al. (2016), the reconnection event must have already  
 555 taken place for the flows to be observed and thus the control is clear. Importantly, we  
 556 also note that too much tail activity, particularly substorms, can inhibit the asymme-  
 557 try observed in ionospheric flows (e.g. Ohma et al., 2018, 2019; Reistad et al., 2018) and  
 558 so we have attempted to address this by filtering by Kp and AL in the SuperDARN plots.

559 We note that our plasma sheet flow data is sampled between  $-14R_E$  and  $-50R_E$ ,  
 560 which is significantly further downtail than the data and modeling used by Tenfjord et  
 561 al. (2015, 2017, 2018). It may be that we simply do not see the prompt reversal response  
 562 further downtail due to the complex nature of the magnetotail, or that this explanation  
 563 does not hold outside of the near-Earth region discussed in Tenfjord et al. (2018). Ad-  
 564 ditionally, we are analysing convection data, rather than the magnetic field data, and there  
 565 is the potential for differences here (e.g. the convection data is a mix of a  $B_y$  component  
 566 being introduced and undone from a previous IMF  $B_y$  state).

## 5 Conclusions

The orientation of the IMF  $B_y$  has previously been shown to exert an influence on the direction of the convection in the magnetotail lobes. Using two complimentary datasets, from in situ spacecraft and ionosphere radars, we confirm that a positive IMF  $B_y$  component drives, on average, positive- $Y_{GSM}$  directed flows in the Northern Hemisphere whilst a negative IMF  $B_y$  component drives negative- $Y_{GSM}$  directed flows. This trend is reversed in the Southern Hemisphere. We note that a flow in the positive- $Y_{GSM}$  direction corresponds to an eastward flow ( $\theta = 90^\circ$ ) in the dayside ionosphere but a westward flow ( $\theta = -90^\circ$ ) in the nightside ionosphere.

We utilise superposed epoch analyses of flow data from the lobes, plasma sheet and ionosphere to rigorously investigate the timing of the magnetosphere-ionosphere system's response to changes in the IMF  $B_y$  component. Particularly, we identified convective flows from these regions that were associated with IMF  $B_y$  reversals to determine how quickly the direction of these flows changed in response to a reversal in the IMF  $B_y$  orientation.

We found that the average flows in the lobes respond promptly to a reversal in the IMF  $B_y$  component, with the flow direction starting to change within 5 min of the IMF  $B_y$  reversals seen in the OMNI data. The average flows reverse in direction around 30-40 min after the IMF  $B_y$  reversal. Additionally, we found that the dayside reconnection rate seems to influence how the lobes respond, with larger reconnection rates ( $\Phi_D > 100$  kV) producing clearer results than smaller rates. Clear and prompt responses were also found with the ionospheric flows at latitudes mapping out to the lobe region ( $\geq 75^\circ$  MLAT), suggesting that changes in the lobes are introduced into the polar cap ionosphere almost instantly. However, in our superposed epoch analyses, the plasma sheet did not respond to reversals in the IMF  $B_y$  component on the timescales used in this study (up to four hours after a reversal). The responses of the associated ionospheric convection data, at  $60^\circ - 70^\circ$  MLAT, were also less clear than their higher-latitude counterparts.

Our result of a prompt response to reversals in the lobes is consistent with both the Cowley and Tenfjord explanations for introducing a  $B_y$  component (and subsequently  $V_y$ ) into the closed field line tail. At first glance, the null result in the plasma sheet appears to be inconsistent with both explanations. However, it is possible that it may actually be consistent with the Cowley explanation due to the nature of the reconnection-driven Dungey cycle complicating any superposed epoch analysis such as ours. Further investigation into the role of tail reconnection adding the IMF  $B_y$  component into the inner magnetotail is needed.

## Acknowledgments

We gratefully acknowledge the various instrument teams from each of the spacecraft missions used in this study. The Cluster data were provided by ESA's Cluster Science Archive (<https://www.cosmos.esa.int/web/csa>). The Geotail data are provided from the Data ARchives and Transmission System (DARTS) of the Institute of Space and Astronautical Science (<https://www.darts.isas.jaxa.jp/stp/geotail/data.html>). The THEMIS data were provided by NASA Goddard Space Flight Center's CDAWeb (<https://cdaweb.sci.gsfc.nasa.gov/>). Solar wind data were provided by NASA GSFC's OMNIWeb database (<https://omniweb.gsfc.nasa.gov/>). The authors acknowledge the use of SuperDARN data. SuperDARN is a collection of radars funded by national scientific funding agencies of Australia, Canada, China, France, Japan, South Africa, United Kingdom, and United States of America, and we thank the international PI team for providing the data. The authors acknowledge access to the SuperDARN database (<http://bsslsuperdarnc.nerc-bas.ac.uk:8093/docs/>) and the Radar Software Toolkit that is used to process the data (<https://zenodo.org/record/1403226#.Xy0u7y3MxTY>).

NAC and AG were supported during this study by STFC grant number ST/R000816/1. RCF was supported by STFC Consolidated Grant ST/R000719/1. SH acknowledges sup-

port from the Norwegian Research Council under grant number 223252. JHL was supported by an FST studentship from Lancaster University.

## References

- Angelopoulos, V. (2009). The THEMIS mission. In J. L. Burch & V. Angelopoulos (Eds.), *The THEMIS mission* (pp. 5–34). New York, NY: Springer New York. doi: 10.1007/978-0-387-89820-9\_2
- Blanc, M. (1988). Magnetosphere-ionosphere coupling. *Computer Physics Communications*, 103–118. doi: 10.1016/0010-4655(88)90219-6
- Borovsky, J. E. (2008). Flux tube texture of the solar wind: Strands of the magnetic carpet at 1 AU? *Journal of Geophysical Research: Space Physics*, 113(A8). doi: 10.1029/2007JA012684
- Browett, S. D., Fear, R. C., Grocott, A., & Milan, S. E. (2017). Timescales for the penetration of IMF By into the Earth’s magnetotail. *Journal of Geophysical Research: Space Physics*, 122(1), 579–593. doi: 10.1002/2016JA023198
- Case, N. A., Grocott, A., Haaland, S., Martin, C. J., & Nagai, T. (2018). Response of Earth’s neutral sheet to reversals in the IMF By component. *Journal of Geophysical Research: Space Physics*, 123(10), 8206–8218. doi: 10.1029/2018JA025712
- Case, N. A., & Wild, J. A. (2012). A statistical comparison of solar wind propagation delays derived from multispacecraft techniques. *J. Geophys. Res.*, 117(A2). doi: 10.1029/2011JA016946
- Chisham, G., Lester, M., Milan, S. E., Freeman, M. P., Bristow, W. A., Grocott, A., . . . Walker, A. D. M. (2007, Jan 01). A decade of the super dual auroral radar network (SuperDARN): scientific achievements, new techniques and future directions. *Surveys in Geophysics*, 28(1), 33–109. doi: 10.1007/s10712-007-9017-8
- Cowley, S. (1981). Magnetospheric asymmetries associated with the y-component of the IMF. *Planetary and Space Science*, 29(1), 79 - 96. doi: https://doi.org/10.1016/0032-0633(81)90141-0
- Cowley, S. W. H., & Lockwood, M. (1992, February). Excitation and decay of solar wind-driven flows in the magnetosphere-ionosphere system. *Annales Geophysicae*, 10, 103–115.
- Dungey, J. W. (1961). Interplanetary magnetic field and the auroral zones. *Phys. Rev. Lett.*, 6(2), 47–48.
- Escoubet, C. P., Schmidt, R., & Goldstein, M. L. (1997). Cluster - science and mission overview. In C. P. Escoubet, C. T. Russell, & R. Schmidt (Eds.), *The Cluster and phoenix missions* (pp. 11–32). Dordrecht: Springer Netherlands. doi: 10.1007/978-94-011-5666-0\_1
- Fear, R. C., & Milan, S. E. (2012). The IMF dependence of the local time of transpolar arcs: Implications for formation mechanism. *Journal of Geophysical Research: Space Physics*, 117(A3). doi: 10.1029/2011JA017209
- Georgescu, E., Puhl-Quinn, P., Vaith, H., Chutter, M., Quinn, J., Paschmann, G., & Torbert, R. (2010). EDI data products in the cluster active archive. In H. Laakso, M. Taylor, & C. P. Escoubet (Eds.), *The cluster active archive* (pp. 83–95). Dordrecht: Springer Netherlands.
- Grocott, A. (2017). Time-dependence of dawn-dusk asymmetries in the terrestrial ionospheric convection pattern. In *Dawndusk asymmetries in planetary plasma environments* (p. 107–123). American Geophysical Union (AGU). doi: 10.1002/9781119216346.ch9
- Grocott, A., & Milan, S. E. (2014). The influence of IMF clock angle timescales on the morphology of ionospheric convection. *Journal of Geophysical Research: Space Physics*, 119(7), 5861–5876. doi: 10.1002/2014JA020136
- Grocott, A., Yeoman, T. K., Milan, S. E., Amm, O., Frey, H. U., Juusola, L., . . .



- 670 Takada, T. (2007). Multi-scale observations of magnetotail flux transport  
 671 during IMF-northward non-substorm intervals. *Annales Geophysicae*, *25*(7),  
 672 1709–1720. doi: 10.5194/angeo-25-1709-2007
- 673 Haaland, S., Paschmann, G., Förster, M., Quinn, J., Torbert, R., Vaith, H., ...  
 674 Kletzing, C. (2008). Plasma convection in the magnetotail lobes: statistical re-  
 675 sults from Cluster EDI measurements. *Annales Geophysicae*, *26*(8), 2371–2382.  
 676 doi: 10.5194/angeo-26-2371-2008
- 677 Haaland, S. E., Paschmann, G., Förster, M., Quinn, J. M., Torbert, R. B., McIlwain,  
 678 C. E., ... Kletzing, C. A. (2007). High-latitude plasma convection from cluster  
 679 edi measurements: method and imf-dependence. *Annales Geophysicae*, *25*(1),  
 680 239–253. doi: 10.5194/angeo-25-239-2007
- 681 Hanuise, C., Senior, C., Cerisier, J. C., Villain, J. P., Greenwald, R. A., Ruohoniemi,  
 682 J. M., & Baker, K. B. (1993). Instantaneous mapping of high-latitude convec-  
 683 tion with coherent HF radars. *Journal of Geophysical Research: Space Physics*,  
 684 *98*(A10), 17387–17400. doi: 10.1029/93JA00813
- 685 Holappa, L., & Mursula, K. (2018). Explicit imf by dependence in high-latitude  
 686 geomagnetic activity. *Journal of Geophysical Research: Space Physics*, *123*(6),  
 687 4728–4740. doi: 10.1029/2018JA025517
- 688 Hori, T., Maezawa, K., Saito, Y., & Mukai, T. (2000). Average profile of ion flow  
 689 and convection electric field in the near-earth plasma sheet. *Geophysical Re-  
 690 search Letters*, *27*(11), 1623–1626. doi: 10.1029/1999GL003737
- 691 Juusola, L., Østgaard, N., & Tanskanen, E. (2011). Statistics of plasma sheet con-  
 692 vection. *Journal of Geophysical Research: Space Physics*, *116*(A8). doi: 10  
 693 .1029/2011JA016479
- 694 Kabin, K., Rankin, R., Marchand, R., Gombosi, T. I., Clauer, C. R., Ridley, A. J.,  
 695 ... DeZeeuw, D. L. (2003). Dynamic response of Earth’s magnetosphere to  
 696 By reversals. *Journal of Geophysical Research: Space Physics*, *108*(A3). doi:  
 697 10.1029/2002JA009480
- 698 Kessel, R. L., Chen, S.-H., Green, J. L., Fung, S. F., Boardsen, S. A., Tan, L. C., ...  
 699 Frank, L. A. (1996). Evidence of high-latitude reconnecting during northward  
 700 imf: Hawkeye observations. *Geophysical Research Letters*, *23*(5), 583–586. doi:  
 701 10.1029/95GL03083
- 702 Khan, H., & Cowley, S. W. H. (1999). Observations of the response time of high-  
 703 latitude ionospheric convection to variations in the interplanetary magnetic  
 704 field using eiscat and imp-8 data. *Annales Geophysicae*, *17*(10), 1306–1335.  
 705 doi: 10.1007/s00585-999-1306-8
- 706 Khurana, K. K., Walker, R. J., & Ogino, T. (1996). Magnetospheric convection in  
 707 the presence of interplanetary magnetic field by : A conceptual model and sim-  
 708 ulations. *Journal of Geophysical Research: Space Physics*, *101*(A3), 4907–4916.  
 709 doi: 10.1029/95JA03673
- 710 King, J. H., & Papitashvili, N. E. (2005). Solar wind spatial scales in and compar-  
 711 isons of hourly Wind and ACE plasma and magnetic field data. *Journal of  
 712 Geophysical Research: Space Physics*, *110*(A2). doi: 10.1029/2004JA010649
- 713 Kissinger, J., McPherron, R. L., Hsu, T.-S., & Angelopoulos, V. (2012). Diver-  
 714 sion of plasma due to high pressure in the inner magnetosphere during steady  
 715 magnetospheric convection. *Journal of Geophysical Research: Space Physics*,  
 716 *117*(A5). doi: 10.1029/2012JA017579
- 717 Liou, K., Sotirelis, T., & Mitchell, E. (2020). Control of the east-west compo-  
 718 nent of the interplanetary magnetic field on the occurrence of magnetic sub-  
 719 storms. *Geophysical Research Letters*, *47*(5), e2020GL087406. (e2020GL087406  
 720 2020GL087406) doi: 10.1029/2020GL087406
- 721 Mailyan, B., Munteanu, C., & Haaland, S. (2008). What is the best method to cal-  
 722 culate the solar wind propagation delay? *Annales Geophysicae*, *26*(8), 2383–  
 723 2394. doi: 10.5194/angeo-26-2383-2008
- 724 McFadden, J. P., Carlson, C. W., Larson, D., Ludlam, M., Abiad, R., Elliott, B.,

- 725 ... Angelopoulos, V. (2008, Dec 01). The THEMIS ESA plasma instru-  
726 ment and in-flight calibration. *Space Science Reviews*, *141*(1), 277–302. doi:  
727 10.1007/s11214-008-9440-2
- 728 Milan, S. E., Evans, T. A., & Hubert, B. (2010). Average auroral configuration pa-  
729 rameterized by geomagnetic activity and solar wind conditions. *Annales Geo-*  
730 *physicae*, *28*(4), 1003–1012. doi: 10.5194/angeo-28-1003-2010
- 731 Milan, S. E., Gosling, J. S., & Hubert, B. (2012). Relationship between interplan-  
732 etary parameters and the magnetopause reconnection rate quantified from  
733 observations of the expanding polar cap. *Journal of Geophysical Research:*  
734 *Space Physics*, *117*(A3). doi: 10.1029/2011JA017082
- 735 Milan, S. E., Grocott, A., & Hubert, B. (2010). A superposed epoch analysis of aur-  
736 oral evolution during substorms: Local time of onset region. *Journal of Geo-*  
737 *physical Research: Space Physics*, *115*(A5). doi: 10.1029/2010JA015663
- 738 Mukai, T., Machida, S., Saito, Y., Hirahara, M., Terasawa, M., Kaya, N., ...  
739 Nishida, A. (1994). The Low Energy Particle (LEP) experiment onboard  
740 the GEOTAIL satellite. *J. Geomag. Geoelectr.*, *46*, 669–692.
- 741 Nishida, A. (1994). The geotail mission. *Geophysical Research Letters*, *21*(25), 2871-  
742 2873. doi: 10.1029/94GL01223
- 743 Ohma, A., Østgaard, N., Reistad, J. P., Tenfjord, P., Laundal, K. M.,  
744 Moretto Jørgensen, T., ... Milan, S. (2019). Observations of asymmetric lobe  
745 convection for weak and strong tail activity. *Journal of Geophysical Research:*  
746 *Space Physics*, *124*(12), 9999-10017. doi: 10.1029/2019JA026773
- 747 Ohma, A., Østgaard, N., Reistad, J. P., Tenfjord, P., Laundal, K. M., Snekvik, K.,  
748 ... Fillingim, M. O. (2018). Evolution of asymmetrically displaced footpoints  
749 during substorms. *Journal of Geophysical Research: Space Physics*, *123*(12),  
750 10,030-10,063. doi: 10.1029/2018JA025869
- 751 Østgaard, N., Mende, S. B., Frey, H. U., Immel, T. J., Frank, L. A., Sigwarth, J. B.,  
752 & Stubbs, T. J. (2004). Interplanetary magnetic field control of the location of  
753 substorm onset and auroral features in the conjugate hemispheres. *Journal of*  
754 *Geophysical Research: Space Physics*, *109*(A7). doi: 10.1029/2003JA010370
- 755 Park, K. S., Ogino, T., & Walker, R. J. (2006). On the importance of antiparallel re-  
756 connection when the dipole tilt and IMF by are nonzero. *Journal of Geophysi-*  
757 *cal Research: Space Physics*, *111*(A5). doi: 10.1029/2004JA010972
- 758 Paschmann, G., Melzner, F., Frenzel, R., Vaith, H., Parigger, P., Pagel, U., ...  
759 Whipple, E. C. (1997, Jan 01). The electron drift instrument for Cluster.  
760 *Space Science Reviews*, *79*(1), 233–269. doi: 10.1023/A:1004917512774
- 761 Petrukovich, A. A., & Lukin, A. S. (2018). Detailed regression model of plasma  
762 sheet by. *Journal of Geophysical Research: Space Physics*, *123*(4), 2872-2883.  
763 doi: 10.1002/2017JA024993
- 764 Pettigrew, E. D., Shepherd, S. G., & Ruohoniemi, J. M. (2010). Climatological  
765 patterns of high-latitude convection in the northern and southern hemispheres:  
766 Dipole tilt dependencies and interhemispheric comparisons. *Journal of Geo-*  
767 *physical Research: Space Physics*, *115*(A7). doi: 10.1029/2009JA014956
- 768 Pitkänen, T., Hamrin, M., Karlsson, T., Nilsson, H., & Kullen, A. (2017). On IMF  
769 by -induced dawn-dusk asymmetries in earthward convective fast flows. In  
770 *Dawndusk asymmetries in planetary plasma environments* (p. 95-106). Ameri-  
771 can Geophysical Union (AGU). doi: 10.1002/9781119216346.ch8
- 772 Pitkänen, T., Hamrin, M., Kullen, A., Maggiolo, R., Karlsson, T., Nilsson, H., &  
773 Norqvist, P. (2016). Response of magnetotail twisting to variations in IMF by:  
774 A THEMIS case study 12 january 2009. *Geophysical Research Letters*, *43*(15),  
775 7822-7830. doi: 10.1002/2016GL070068
- 776 Pitkänen, T., Hamrin, M., Norqvist, P., Karlsson, T., & Nilsson, H. (2013). IMF de-  
777 pendence of the azimuthal direction of earthward magnetotail fast flows. *Geo-*  
778 *physical Research Letters*, *40*(21), 5598-5604. doi: 10.1002/2013GL058136
- 779 Pitkänen, T., Kullen, A., Laundal, K. M., Tenfjord, P., Shi, Q. Q., Park, J.-S., ...

- 780 Tian, A. M. (2019). IMF By influence on magnetospheric convection in Earth's  
 781 magnetotail plasma sheet. *Geophysical Research Letters*, *46*(21), 11698-11708.  
 782 doi: 10.1029/2019GL084190
- 783 Reistad, J. P., Laundal, K. M., Ohma, A., Moretto, T., & Milan, S. E. (2020).  
 784 An explicit imf b dependence on solar wind-magnetosphere coupling.  
 785 *Geophysical Research Letters*, *47*(1), e2019GL086062. (e2019GL086062  
 786 10.1029/2019GL086062) doi: 10.1029/2019GL086062
- 787 Reistad, J. P., Østgaard, N., Laundal, K. M., Ohma, A., Snekvik, K., Tenfjord, P.,  
 788 ... Haaland, S. (2018). Observations of asymmetries in ionospheric return  
 789 flow during different levels of geomagnetic activity. *Journal of Geophysical*  
 790 *Research: Space Physics*, *123*(6), 4638-4651. doi: 10.1029/2017JA025051
- 791 Reistad, J. P., Østgaard, N., Laundal, K. M., & Oksavik, K. (2013). On the non-  
 792 conjugacy of nightside aurora and their generator mechanisms. *Journal of Geo-*  
 793 *physical Research: Space Physics*, *118*(6), 3394-3406. doi: 10.1002/jgra.50300
- 794 Rème, H., Aoustin, C., Bosqued, J. M., Dandouras, I., Lavraud, B., Sauvaud, J. A.,  
 795 ... Sonnerup, B. (2001). First multispacecraft ion measurements in and  
 796 near the Earths magnetosphere with the identical Cluster ion spectrome-  
 797 try (CIS) experiment. *Annales Geophysicae*, *19*(10/12), 1303-1354. doi:  
 798 10.5194/angeo-19-1303-2001
- 799 Ruohoniemi, J. M., & Baker, K. B. (1998). Large-scale imaging of high-latitude con-  
 800 vection with super dual auroral radar network hf radar observations. *Journal*  
 801 *of Geophysical Research: Space Physics*, *103*(A9), 20797-20811. doi: 10.1029/  
 802 98JA01288
- 803 Ruohoniemi, J. M., & Greenwald, R. A. (2005). Dependencies of high-latitude  
 804 plasma convection: Consideration of interplanetary magnetic field, seasonal,  
 805 and universal time factors in statistical patterns. *Journal of Geophysical Re-*  
 806 *search: Space Physics*, *110*(A9). doi: 10.1029/2004JA010815
- 807 Russell, C. T. (1972). The configuration of the magnetosphere. In E. Dyer (Ed.),  
 808 *Critical problems of magnetospheric physics* (pp. 1-16). Washington, D. C.:  
 809 National Academy of Sciences.
- 810 Tenfjord, P., Østgaard, N., Haaland, S., Snekvik, K., Laundal, K. M., Reistad, J. P.,  
 811 ... Ohma, A. (2018). How the IMF By induces a local By component dur-  
 812 ing northward IMF Bz and characteristic timescales. *Journal of Geophysical*  
 813 *Research: Space Physics*, *123*(5), 3333-3348. doi: 10.1002/2018JA025186
- 814 Tenfjord, P., Østgaard, N., Snekvik, K., Laundal, K. M., Reistad, J. P., Haaland, S.,  
 815 & Milan, S. E. (2015). How the IMF By induces a By component in the closed  
 816 magnetosphere and how it leads to asymmetric currents and convection pat-  
 817 terns in the two hemispheres. *Journal of Geophysical Research: Space Physics*,  
 818 *120*(11), 9368-9384. doi: 10.1002/2015JA021579
- 819 Tenfjord, P., Østgaard, N., Strangeway, R., Haaland, S., Snekvik, K., Laundal,  
 820 K. M., ... Milan, S. E. (2017). Magnetospheric response and reconfiguration  
 821 times following IMF By reversals. *Journal of Geophysical Research: Space*  
 822 *Physics*, *122*(1), 417-431. doi: 10.1002/2016JA023018
- 823 Thomas, E. G., & Shepherd, S. G. (2018). Statistical patterns of ionospheric con-  
 824 vection derived from mid-latitude, high-latitude, and polar SuperDARN HF  
 825 radar observations. *Journal of Geophysical Research: Space Physics*, *123*(4),  
 826 3196-3216. doi: 10.1002/2018JA025280
- 827 Vokhmyanin, M. V., Stepanov, N. A., & Sergeev, V. A. (2019). On the evalua-  
 828 tion of data quality in the OMNI interplanetary magnetic field database. *Space*  
 829 *Weather*, *17*(3), 476-486. doi: 10.1029/2018SW002113

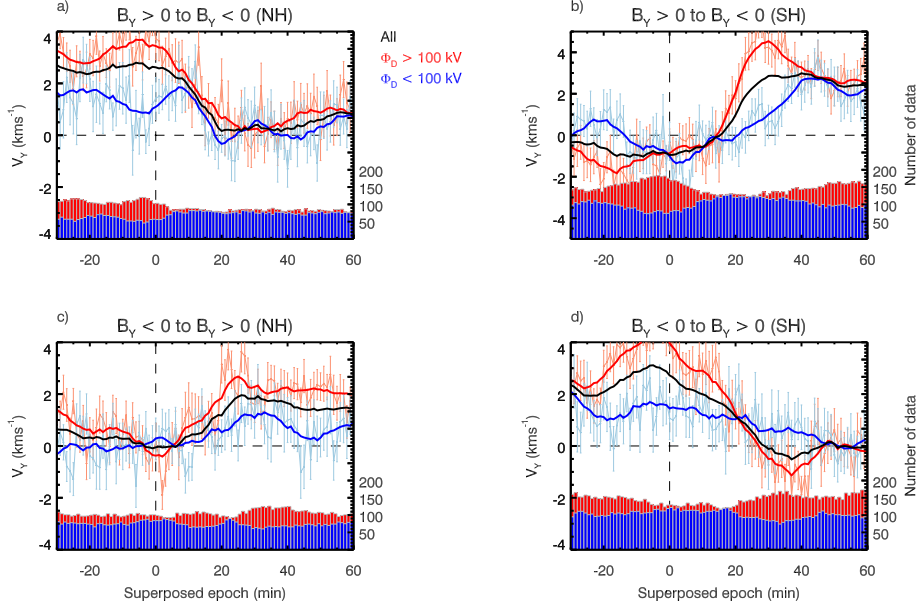


**Figure 4.** In a similar format as Figure 1, superposed epoch Cluster-EDI velocity data sampled in the lobes are shown for (a and b) IMF  $B_y$  positive to negative reversals and for (c and d) IMF  $B_y$  negative to positive reversals. (a and c) Northern Hemisphere (NH) and (b and d) Southern Hemisphere (SH) data are shown respectively. Plotted in blue and red are data for  $\Phi_D < 100$  kV and  $\Phi_D > 100$  kV respectively. The number of data points for each subset are shown by the histogram bars.

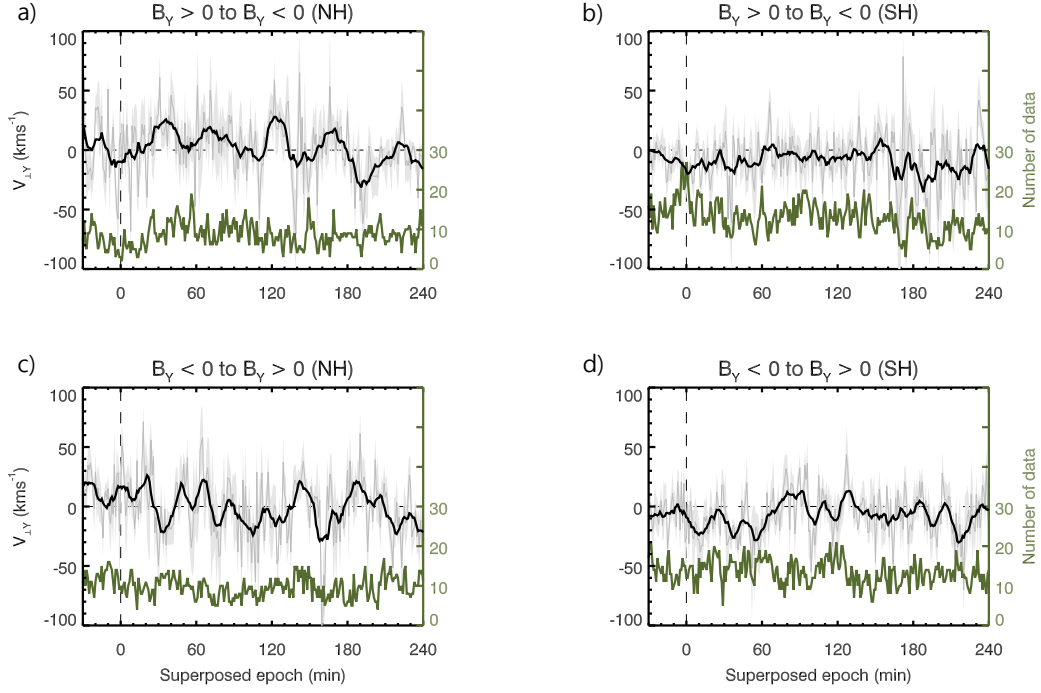


**Figure 5.** Superposed epoch plasma sheet velocity data are shown for (a and b) IMF  $B_y$  positive to negative reversals and for (c and d) IMF  $B_y$  negative to positive reversals. (a and c) Northern Hemisphere (NH) and (b and d) Southern Hemisphere (SH) data are shown respectively. Plotted in black are the superposed means for all data. The gray shaded region indicates the standard error of the mean for each timestamp. The number of data points for each superposed average timestamp is shown by the olive green line on the secondary y-axis.

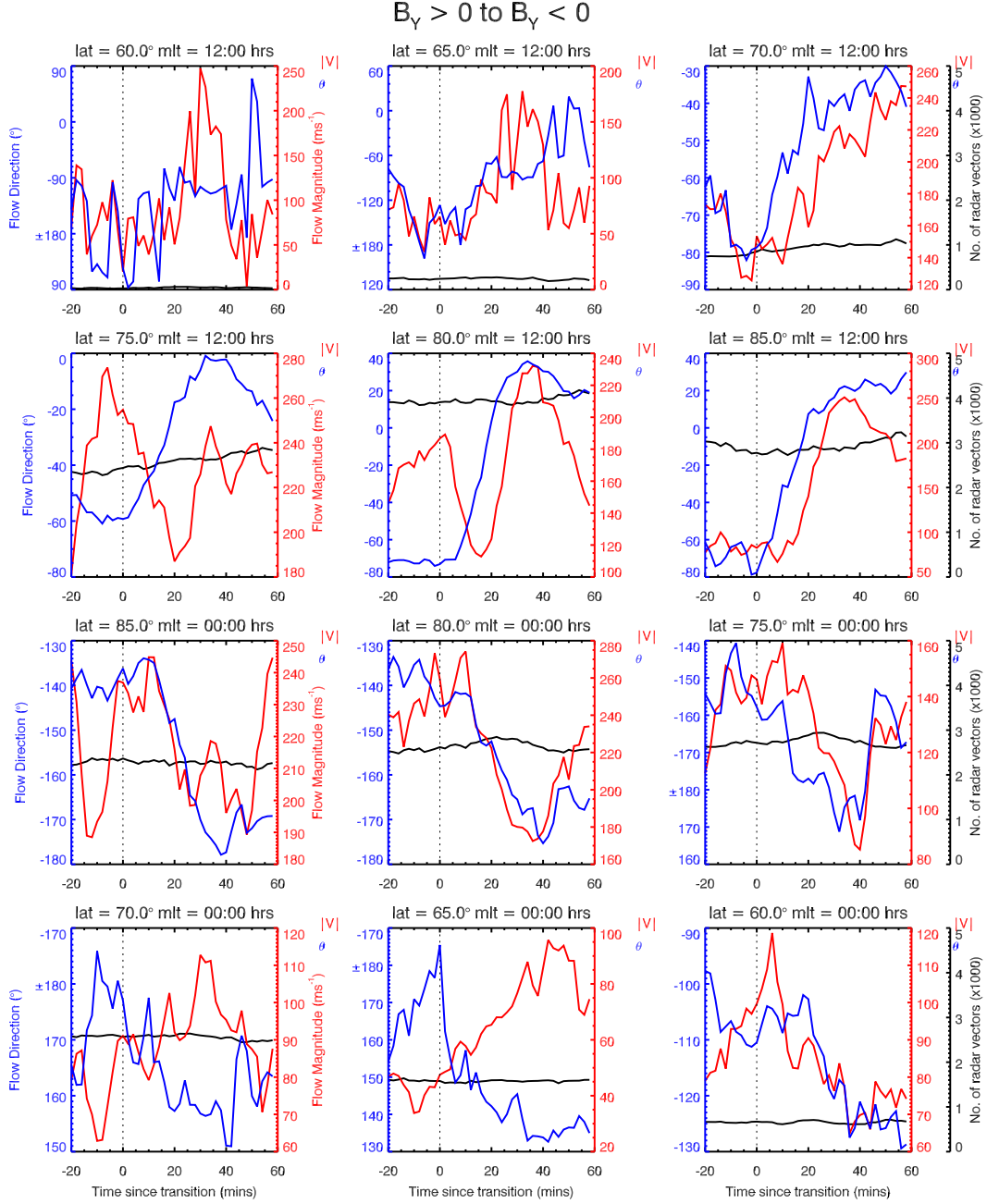


**Figure 6.** Superposed epoch SuperDARN ionospheric flows, recorded in the Northern Hemisphere, along the noon-midnight meridian (MLT) across the polar cap from  $60^\circ$  MLAT on the dayside to  $60^\circ$  MLAT on the nightside. Data correspond to a positive to negative IMF  $B_y$  reversal. Plotted in red is the median flow speed and in blue is the median flow direction. The number of vectors for each superposed average time stamp is shown by the black line on the secondary axis. The secondary axis has been scaled down by 1000, i.e. 5 = 5,000 vectors.

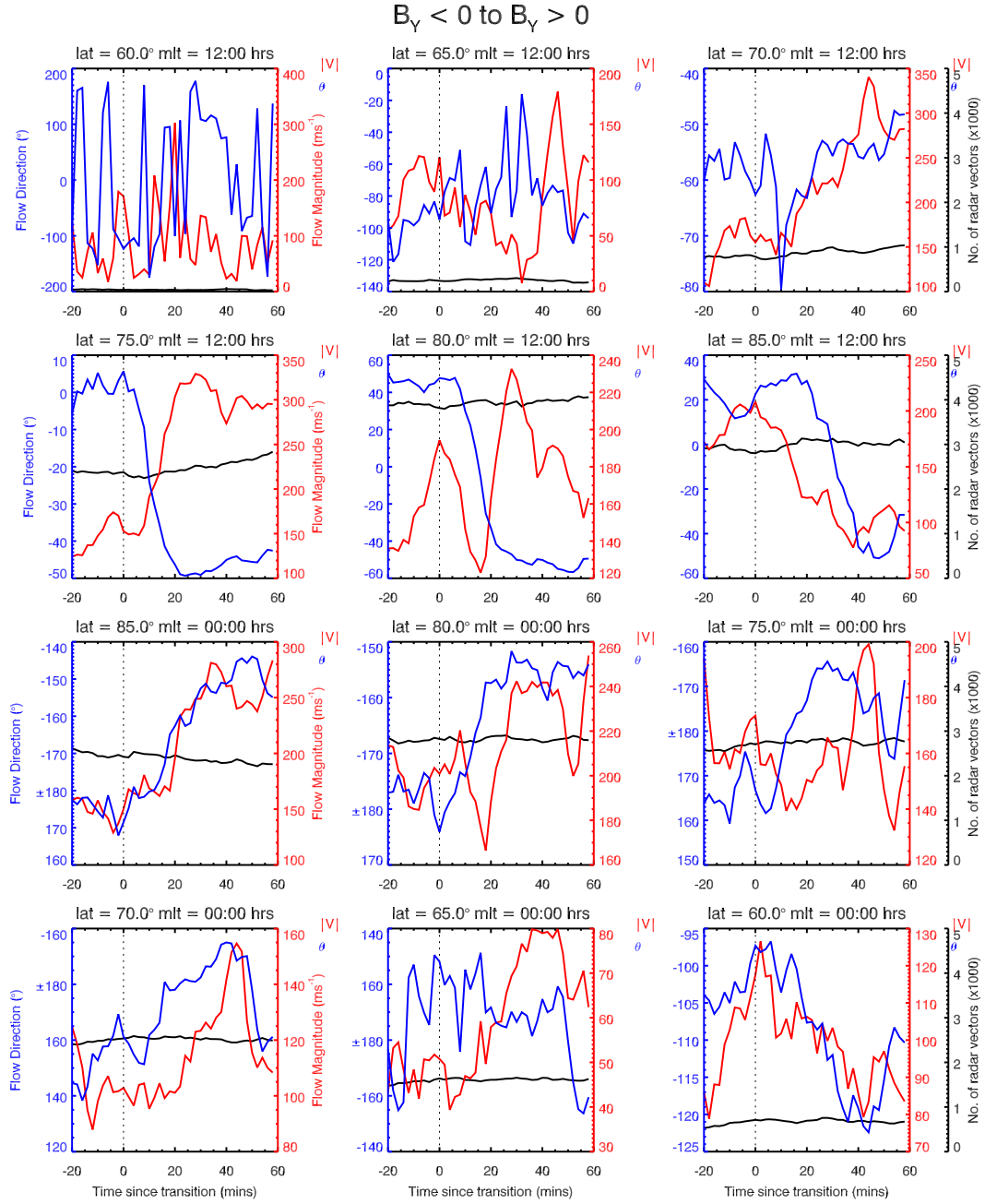


**Figure 7.** As Figure 6, but with superposed epoch SuperDARN ionospheric flows corresponding to a negative to positive IMF  $B_y$  reversal.